

[

The resistance and mobility functions for spheres in low-Reynolds-number flow

Baopi Liu^{1*}, Lu Chen², Ji Zhang³, Xin-Liang Xu^{1,2*}

Abstract

The resistance and mobility matrix completely characterize the linear relations between the forces and torques and the translational and rotational velocities of the multi-sphere system in low Reynolds number fluids. These relations may be represented completely by either a set of 10 resistance functions or a set of 10 mobility functions [J. Fluid Mech. **139**, 261 (1984)]. These functions provides precise dependent couplings of hydrodynamic force and torque to sphere translation and rotation. Here, we calculate continuous resistance and mobility matrix, which contains near-field lubrication and far-field interactions, which allows us to study the collective behavior of multi-spheres with accurate hydrodynamic interactions when they touch one another. The three main merits of this approximation are that it avoids overlap, satisfies the no-slip boundary condition, and includes all long-range terms. Additionally, the propulsion force and torque of a helical rigid flagellum calculated are shown to agree well with the result of Rodenborn's work [PNAS, **110**(5): E338-E347 (2013)], which verifies the accuracy of the resistance matrix constructed here.

Keywords

Low Reynolds number — Resistance matrix — Mobility matrix — Lubrication

¹ Beijing Computational Science Research Center, Beijing, 100193, China² Department of Physics, Beijing Normal University, Beijing, 100875, China³ Zhejiang Lab, Hangzhou, 310027, China

*Corresponding author: bpliu@mail.bnu.edu.cn, xinliang@csrc.ac.cn

]

Contents

1	Introduction	1
2	The Resistance and Mobility Matrix	2
3	Propulsion of a Helical Rigid Flagellum	7
4	Summary and Conclusions	7
	Acknowledgments	8
	Appendix A. The scalar resistance and mobility functions	9
	References	9

1. Introduction

Many situations in nature and technology involve the motion of rigid spheres immersed in a viscous fluid[1, 2, 3]. The motion of each sphere in the fluid causes a flow pattern[4], which in turn affects the motion of other spheres[5, 6]. The behavior of a finite number of spheres suspended or dispersed in a viscous fluid, subject to externally imposed forces, torques, or a linear shear flow, is fundamental to low Reynolds number hydrodynamics. Which occur in a variety of natural and man-made systems such as bacteria[7], suspensions[8], colloids[9], polymers[10, 11] and artificial microswimmers[12], etc. Hydrodynamic interactions between rigid spheres have been studied by many authors. Several methods have been developed for solving the equations of low Reynolds number fluids around two spheres[13, 14, 15]. The problem of hydrodynamic interaction between multi-spheres is, however, complicated compared with the interactions of two spheres.

The Rotne-Prager-Yamakawa (RPY) approximation[16, 17] is one of the most commonly used methods in modeling multi-sphere systems[10, 18, 19, 20]. The Rotne-Prager-Yamakawa tensor is a far-field approximation, which is accurate

at long distances (decaying as fast as the inverse third power or slower of the inter-sphere distances, which coincide with the far-field mobility matrix truncated at $q = 3$ order in Jeffrey and Onishi[13]), but is less accurate at smaller distances. In particular, the Rotne-Prager-Yamakawa tensor can't avoid the overlap of spheres, and the hydrodynamic tensors calculated based on the Rotne-Prager-Yamakawa tensor in this case may become non-positive definite, which leads to numerical problems in the Brownian dynamics simulations[21, 22]. Durlofsky et al. presented a general method of computing the hydrodynamic interactions among N spheres under the condition of low Reynolds numbers, $\mathcal{R} = (\mathcal{M}^\infty)^{-1} + \mathcal{R}_{2B} - \mathcal{R}_{2B}^\infty$ [23, 24, 25], which is referred to as Stokesian dynamics. This method is, however, in terms of a finite series, which is computationally expensive, and the inverse of this grand resistance matrix $\mathcal{M} = (\mathcal{R})^{-1}$ may diverge. To avoid this, a new approach is needed.

Determining the motion of spheres in unbounded flow is a central problem in the world of microhydrodynamics[1]. The purpose of this paper is to present an efficient method of accurately calculating the grand resistance and mobility matrix. A simple, direct method that provides accurate information on the grand resistance functions of unequal spheres at all separations, including the case of touching, is introduced. In addition, the multi-sphere mobility matrix is the key quantity required in both the Stokesian dynamics and Brownian dynamics simulations of finite clusters of particles moving under prescribed forces and torques[7, 26, 27]. The resistance matrix obtained from the inverse of the Rotne-Prager-Yamakawa tensor still lacks, however, lubrication interactions. Lubrication interactions would only be reproduced upon inversion of the mobility matrix if all multipole moments were included. To include lubrication interactions, we introduce them in a pairwise additive fashion in the resistance matrix. We continue a program started in Jeffrey and Onishi that aims to calculate all the resistance functions and mobility functions in a uniform manner, which is referred to as the multipole moment method (MMM)[23, 24, 25]. The strategy of the multipole moment method to save computational costs is that it only calculates the relationship between the forces on particles and their velocity, without caring about how the flow field around particles changes.

This paper is organized as follows: in Section 2, we describe the process of constructing the grand resistance matrix and the inverse of it to obtain the grand mobility matrix. Then it was demonstrated that the grand resistance matrix satisfies the overlap-avoiding and no-slip boundary conditions[28]. Flagella can be formed by a chain of beads attached to one another by rigid rods[29, 30]. The propulsion force and torque of a helical rigid flagellum are obtained, which verifies the accuracy of the grand resistance matrix in Section 3. Finally, discussions and some perspectives on future work are presented in Section 4.

2. The Resistance and Mobility Matrix

The three-dimensional flow around the spheres has a low Reynolds number and is governed by incompressible Stokes equations, which are given by:[31, 32]:

$$\begin{aligned} \mu \nabla^2 \mathbf{u} - \nabla p + \mathbf{f} &= 0, \\ \nabla \cdot \mathbf{u} &= 0 \end{aligned} \quad (1)$$

where μ is the dynamic viscosity, \mathbf{u} is the fluid velocity, p is the pressure, and \mathbf{f} is the force applied to the fluid by the immersed body. The Stokes solutions provide a good approximation to the flow field near a body when the Reynolds number, $Re = \rho UL/\mu$, is small. Here ρ , U and L are the fluid density, sphere velocity, and sphere dimension, respectively[31]. Due to the linearity of the Stokes equations, the force \mathbf{F} and torque \mathbf{T} that spheres exert on the fluid depend linearly on the translational velocity \mathbf{U} and angular velocity $\mathbf{\Omega}$ of the spheres. On account of the linearity of the Stokes equations, the resistance matrix that relates forces and torques to the translational and angular velocities of N spheres is[23, 24, 25]:

$$\begin{pmatrix} \mathbf{F} \\ \mathbf{T} \end{pmatrix} = \mathcal{R} \begin{pmatrix} \mathbf{U} - \mathbf{U}^\infty \\ \mathbf{\Omega} - \mathbf{\Omega}^\infty \end{pmatrix}. \quad (2)$$

where \mathbf{U}^∞ and $\mathbf{\Omega}^\infty$ are the ambient flow fields and $\mathbf{U} - \mathbf{U}^\infty$ and $\mathbf{\Omega} - \mathbf{\Omega}^\infty$ are vectors of dimension $3N$ of all N spheres relative to the ambient flow. The inverse problem is to calculate the velocities of spheres given their forces and torques:

$$\begin{pmatrix} \mathbf{U} \\ \mathbf{\Omega} \end{pmatrix} = \begin{pmatrix} \mathbf{U}^\infty \\ \mathbf{\Omega}^\infty \end{pmatrix} + \mathcal{M} \begin{pmatrix} \mathbf{F} \\ \mathbf{T} \end{pmatrix}. \quad (3)$$

Consider a set of N rigid spheres of arbitrary size immersed in a viscous fluid. Using the multipole moment method, the grand resistance matrix \mathcal{R} , which contains both near-field lubrication and far-field interactions, can be constructed as

$$\mathcal{R} = (\mathcal{M}^\infty)^{-1} + \mathcal{R}_{2B, \text{lub}}. \quad (4)$$

where the subscript letter 'lub' indicates 'lubrication'. The grand resistance matrix includes both the multi-sphere far-field interactions via the inversion of \mathcal{M}^∞ (which is consistent with the expression of the RPY tensor) and the pairwise lubrication

interactions $\mathcal{R}_{2B,lub}$. The multi-sphere far-field mobility matrix \mathcal{M}^∞ is shown as

$$\mathcal{M}^\infty = \begin{pmatrix} \mathbf{M}_{\alpha\beta}^{tt} & \mathbf{M}_{\alpha\beta}^{tr} \\ \mathbf{M}_{\alpha\beta}^{rt} & \mathbf{M}_{\alpha\beta}^{rr} \end{pmatrix}. \quad (5)$$

\mathcal{M}^∞ is a far-field approximation to the interaction among spheres and includes terms up to $O(s^{-3})$, which is the same as the result of the Rotne-Prager-Yamakawa (RPY) tensor. The detailed elements of \mathcal{M}^∞ are given explicitly in [Appendix A](#) using the notation of Jeffrey and Onishi (1984). The inverse of \mathcal{M}^∞ will include multi-sphere interactions. The pairwise near-field lubrication resistance matrix is denoted as $\mathcal{R}_{2B,lub}$ and constructed as

$$\mathcal{R}_{2B,lub} = \begin{pmatrix} \mathbf{R}_{\alpha\beta}^{tt} & \mathbf{R}_{\alpha\beta}^{tr} \\ \mathbf{R}_{\alpha\beta}^{rt} & \mathbf{R}_{\alpha\beta}^{rr} \end{pmatrix}. \quad (6)$$

for $\xi \leq \min\{\lambda, 1/\lambda\}$ and set to a zero matrix for $\xi > \min\{\lambda, 1/\lambda\}$. The segmentation point of near- and far-field can be smaller than $\xi \leq \min\{\lambda, 1/\lambda\}$. $\mathcal{R}_{2B,lub}$ is a continuous function of variable s and tends to zero when $s \rightarrow 2 + \min\{\lambda, 1/\lambda\}$ to ensure the continuity of the matrix. This procedure captures both near- and far-field interactions and has saved on computational costs.

We follow the notation of Jeffrey and Onishi and define the variables $s = 2r/(a_\alpha + a_\beta)$, $\xi = s - 2$, and $\lambda = a_\beta/a_\alpha$ (the subscripts α and β indicate the labels of the spheres), where r is the center-to-center distance of the inter-sphere and a_α is the radius of sphere α . Then $\mathbf{e}_{\alpha\beta} = (\mathbf{x}_\alpha - \mathbf{x}_\beta) / |\mathbf{x}_\alpha - \mathbf{x}_\beta|$ is the unit vector along the line of centers. The submatrices $\mathbf{R}_{\alpha\beta}^{tt}$, $\mathbf{R}_{\alpha\beta}^{tr}$, $\mathbf{R}_{\alpha\beta}^{rt}$, $\mathbf{R}_{\alpha\beta}^{rr}$, $\mathbf{M}_{\alpha\beta}^{tt}$, $\mathbf{M}_{\alpha\beta}^{tr}$, $\mathbf{M}_{\alpha\beta}^{rt}$, and $\mathbf{M}_{\alpha\beta}^{rr}$ are second-rank tensors, and the dimensional expression can be expressed as follows, respectively

$$\begin{aligned} \mathbf{R}_{\alpha\beta}^{tt} &= 3\pi\mu(a_\alpha + a_\beta) \left[X_{\alpha\beta}^a \mathbf{e}_{\alpha\beta} \otimes \mathbf{e}_{\alpha\beta} + Y_{\alpha\beta}^a (\mathbb{I} - \mathbf{e}_{\alpha\beta} \otimes \mathbf{e}_{\alpha\beta}) \right], \\ \mathbf{R}_{\alpha\beta}^{tr} &= \pi\mu(a_\alpha + a_\beta)^2 Y_{\alpha\beta}^b (\mathbf{e}_{\beta\alpha} \times), \\ \mathbf{R}_{\alpha\beta}^{rt} &= \pi\mu(a_\alpha + a_\beta)^2 Y_{\alpha\beta}^b (\mathbf{e}_{\alpha\beta} \times), \\ \mathbf{R}_{\alpha\beta}^{rr} &= \pi\mu(a_\alpha + a_\beta)^3 \left[X_{\alpha\beta}^c \mathbf{e}_{\alpha\beta} \otimes \mathbf{e}_{\alpha\beta} + Y_{\alpha\beta}^c (\mathbb{I} - \mathbf{e}_{\alpha\beta} \otimes \mathbf{e}_{\alpha\beta}) \right]. \end{aligned} \quad (7)$$

and

$$\begin{aligned} \mathbf{M}_{\alpha\beta}^{tt} &= \frac{1}{3\pi\mu(a_\alpha + a_\beta)} \left[x_{\alpha\beta}^a \mathbf{e}_{\alpha\beta} \otimes \mathbf{e}_{\alpha\beta} + y_{\alpha\beta}^a (\mathbb{I} - \mathbf{e}_{\alpha\beta} \otimes \mathbf{e}_{\alpha\beta}) \right], \\ \mathbf{M}_{\alpha\beta}^{tr} &= \frac{1}{\pi\mu(a_\alpha + a_\beta)^2} y_{\alpha\beta}^b (\mathbf{e}_{\beta\alpha} \times), \\ \mathbf{M}_{\alpha\beta}^{rt} &= \frac{1}{\pi\mu(a_\alpha + a_\beta)^2} y_{\alpha\beta}^b (\mathbf{e}_{\alpha\beta} \times), \\ \mathbf{M}_{\alpha\beta}^{rr} &= \frac{1}{\pi\mu(a_\alpha + a_\beta)^3} \left[x_{\alpha\beta}^c \mathbf{e}_{\alpha\beta} \otimes \mathbf{e}_{\alpha\beta} + y_{\alpha\beta}^c (\mathbb{I} - \mathbf{e}_{\alpha\beta} \otimes \mathbf{e}_{\alpha\beta}) \right]. \end{aligned} \quad (8)$$

where \mathbb{I} is the 3×3 identity matrix and $(\mathbf{e} \times)$ is the antisymmetric 3×3 matrix defined by $(\mathbf{e} \times) \mathbf{v} = \mathbf{e} \times \mathbf{v}$ for any \mathbf{v} . The elements of the matrix obey a number of symmetry conditions, which are given in Jeffrey and Onishi. The specific expressions of resistance matrix and mobility matrix functions are provided in [Appendix A](#). The grand resistance matrix \mathcal{R} written in terms of individual elements in the notation of Jeffrey and Onishi is

$$\mathcal{R} = \begin{pmatrix} \mathcal{R}_{\alpha\beta}^{tt} & \mathcal{R}_{\alpha\beta}^{tr} \\ \mathcal{R}_{\alpha\beta}^{rt} & \mathcal{R}_{\alpha\beta}^{rr} \end{pmatrix}. \quad (9)$$

where the submatrices are expressed as:

$$\begin{aligned} \mathcal{R}_{\alpha\beta}^{tt} &= 3\pi\mu(a_\alpha + a_\beta) \left[X_{\alpha\beta}^A \mathbf{e}_{\alpha\beta} \otimes \mathbf{e}_{\alpha\beta} + Y_{\alpha\beta}^A (\mathbb{I} - \mathbf{e}_{\alpha\beta} \otimes \mathbf{e}_{\alpha\beta}) \right], \\ \mathcal{R}_{\alpha\beta}^{tr} &= \pi\mu(a_\alpha + a_\beta)^2 Y_{\alpha\beta}^B (\mathbf{e}_{\beta\alpha} \times), \\ \mathcal{R}_{\alpha\beta}^{rt} &= \pi\mu(a_\alpha + a_\beta)^2 Y_{\alpha\beta}^B (\mathbf{e}_{\alpha\beta} \times), \\ \mathcal{R}_{\alpha\beta}^{rr} &= \pi\mu(a_\alpha + a_\beta)^3 \left[X_{\alpha\beta}^C \mathbf{e}_{\alpha\beta} \otimes \mathbf{e}_{\alpha\beta} + Y_{\alpha\beta}^C (\mathbb{I} - \mathbf{e}_{\alpha\beta} \otimes \mathbf{e}_{\alpha\beta}) \right]. \end{aligned} \quad (10)$$

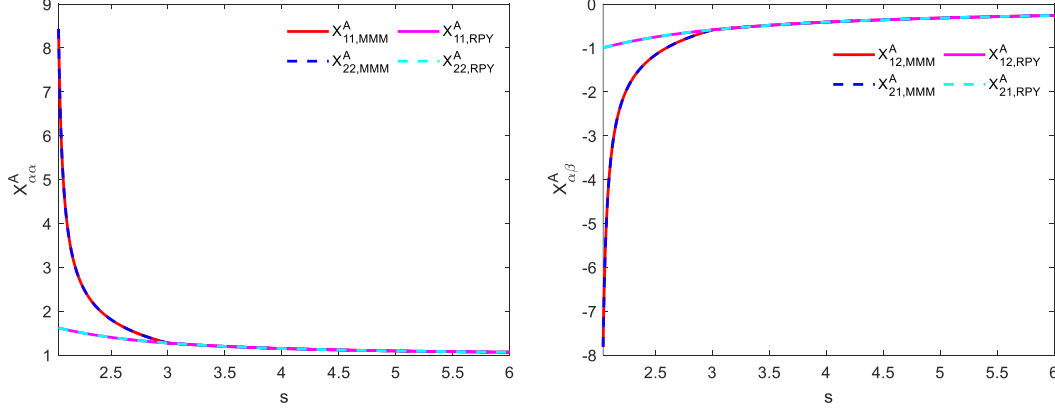


Figure 1. Longitudinal resistance functions by coupling force on the surface of a sphere to the motion of that and other spheres. Comparison of the multipole moment method (MMM) and the Rotne-Prager-Yamakawa (RPY) tensor for scalar resistance functions $X_{\alpha\beta}^A$ as a function of s .

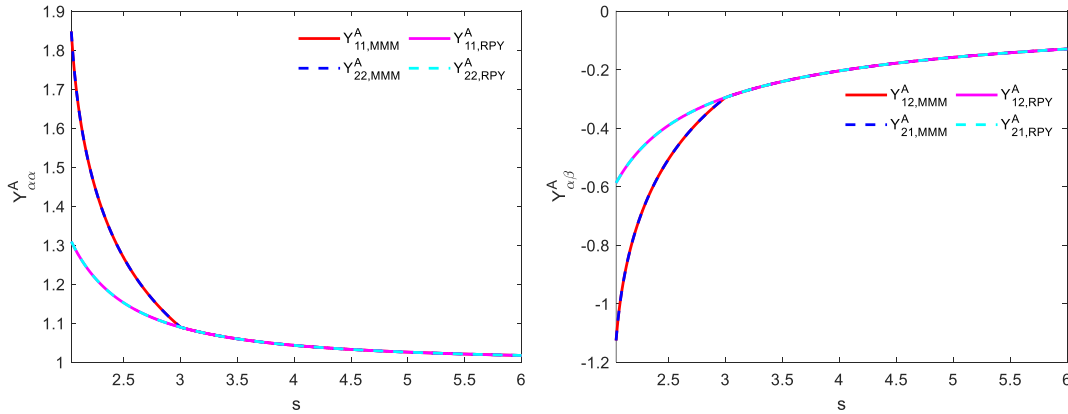


Figure 2. Transverse resistance functions by coupling force on the surface of a sphere to the motion of that and other spheres. Comparison of the multipole moment method (MMM) and the Rotne-Prager-Yamakawa (RPY) tensor for scalar resistance functions $Y_{\alpha\beta}^A$ as a function of s .

The scalar resistance functions X^A , Y^A , Y^B , X^C , and Y^C are plotted versus the reduced sphere-sphere separation distance, $s = 2r/(a_\alpha + a_\beta)$, in Figures 1-5, respectively. The grand mobility matrix is the inverse of the grand resistance matrix

$$\mathcal{M} = \mathcal{R}^{-1}. \quad (11)$$

The grand mobility matrix \mathcal{M} obtained by this method is convergent at any separation distance s . For near-field lubrication, the term ξ^{-1} is introduced to ensure overlap-avoiding, and the term $\log(\xi^{-1})$ is introduced to include the relation between the rotational motion and the force and torque.

We examine the results for the resistance functions and compare them, where available, with those obtained by the RPY tensor. Several resistance functions are plotted versus the reduced separation distance, s , in Figures 1-5, respectively. These plots were generated for s between $2.0 \leq s \leq 6.0$. The longitudinal components X^A of the resistance matrix \mathcal{R}^{tt} are plotted in Figure 1, which couple forces and translational velocities along the line of centers. When the spheres touch, that is, $s = 2$, the scalar resistance functions X^A tend to infinity, which automatically avoids the overlapping of two spheres. These components, which include near-field lubrication, are far different from the components of the RPY tensor. The transverse components Y^A of the resistance matrix \mathcal{R}^{tt} are plotted in Figure 2, which couple forces and translational velocities perpendicular to the line of centers.

The resistance functions Y^B in Figure 3 couple sphere forces to rotational velocities or sphere torques to translational velocities. The longitudinal components X^C of the resistance matrix \mathcal{R}^{rr} are plotted in Figure 4, which couple torques and rotational velocities along the line of centers. Figure 4 shows that the resistance functions X^C obtained by the multipole moment

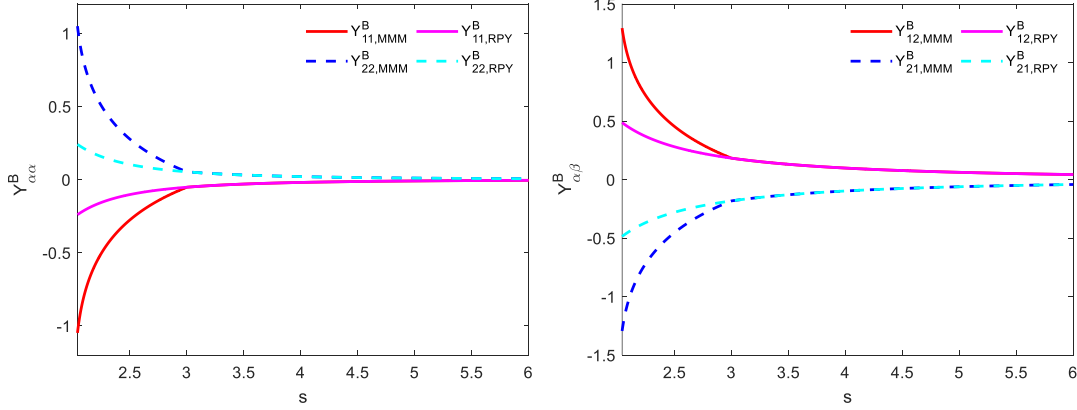


Figure 3. Comparison of the multipole moment method (MMM) and the Rotne-Prager-Yamakawa (RPY) tensor for scalar resistance functions $Y_{\alpha\beta}^B$ as a function of s .

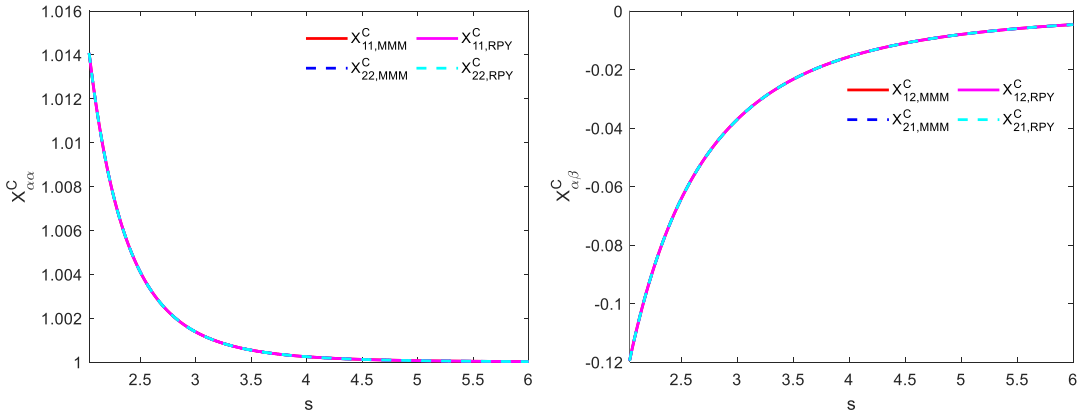


Figure 4. Longitudinal resistance functions by coupling force on the surface of a sphere to the motion of that and other spheres. Comparison of the multipole moment method (MMM) and the Rotne-Prager-Yamakawa (RPY) tensor for scalar resistance functions $X_{\alpha\beta}^C$ as a function of s .

method (MMM) and the Rotne-Prager-Yamakawa (RPY) tensor are the same. And the transverse components Y^C of the resistance matrix \mathcal{R}^{rr} are plotted in Figure 5, which couple torques and rotational velocities perpendicular to the line of centers.

As an example, in Figure 6 (a) we compare the translational velocities of two equal spheres dragged by forces \mathbf{F} and $-\mathbf{F}$ computed by the grand resistance matrix and RPY tensor, respectively. Rather than moving very slowly toward one another, two spheres would physically touch and overlap if there were no other repulsive forces present to prevent contact. Using the grand resistance matrix, we find that the translational velocity tends to 0 near $s = 2$, which is very different from the result obtained by the RPY tensor. The grand resistance matrix constructed here automatically prevents the overlapping of spheres, enabling us not to need to introduce repulsive potential.[10, 11, 18, 19, 20, 33].

The prediction of the no-slip boundary condition is $[(U_y^1 - U_y^2) + a(\Omega_z^1 + \Omega_z^2)] / (U_y^1(\infty) - U_y^2(\infty)) = 0$ at $s = 2$. In order to demonstrate fulfillment of the no-slip boundary condition of this grand resistance matrix, two equal spheres are lined along the x axis and then exert forces F and $-F$ on the two spheres along the y axis, respectively. We qualitatively produce the dimensionless no-slip boundary condition, $[(U_y^1 - U_y^2) + a(\Omega_z^1 + \Omega_z^2)] / (U_y^1(\infty) - U_y^2(\infty)) \leq 1$ (the subscript indicates the axis and superscript indicates the sphere), which is shown in Figure 6 (b). The numerical simulation is found to match our prediction at small separation $s \rightarrow 2$. This means that the no-slip boundary condition has been achieved at the point 'A' of closest approach, and the lateral translation vanishes, but rotation is still possible. The reason why the result slightly deviates from 0 when $s \rightarrow 2$ is that we neglect the term $\xi \log(1/\xi)$ when calculating the matrix $\mathcal{R}_{2B, lub}$. Which will increase the computational cost but have little impact on the results. The result calculated by the Rotne-Prager-Yamakawa (RPY) tensor is far different from our prediction.

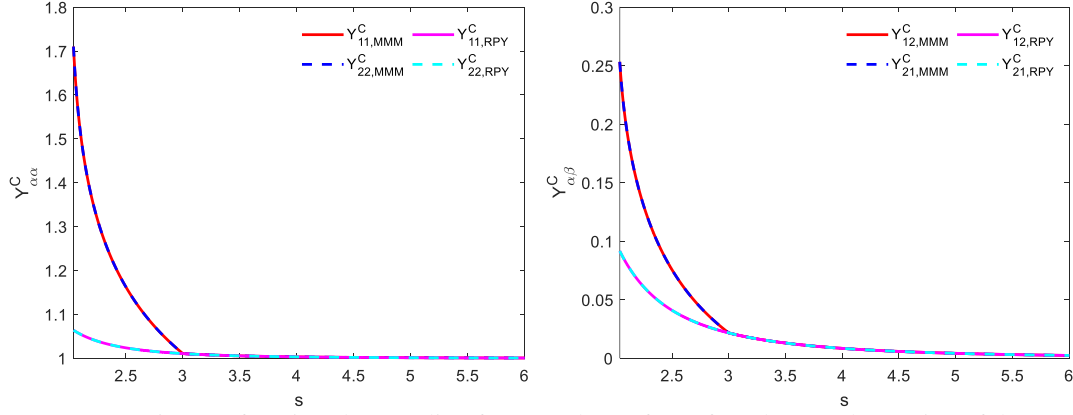


Figure 5. Transverse resistance functions by coupling force on the surface of a sphere to the motion of that and other spheres. Comparison of the multipole moment method (MMM) and the Rotne-Prager-Yamakawa (RPY) tensor for scalar resistance functions $Y_{\alpha\beta}^C$ as a function of s .

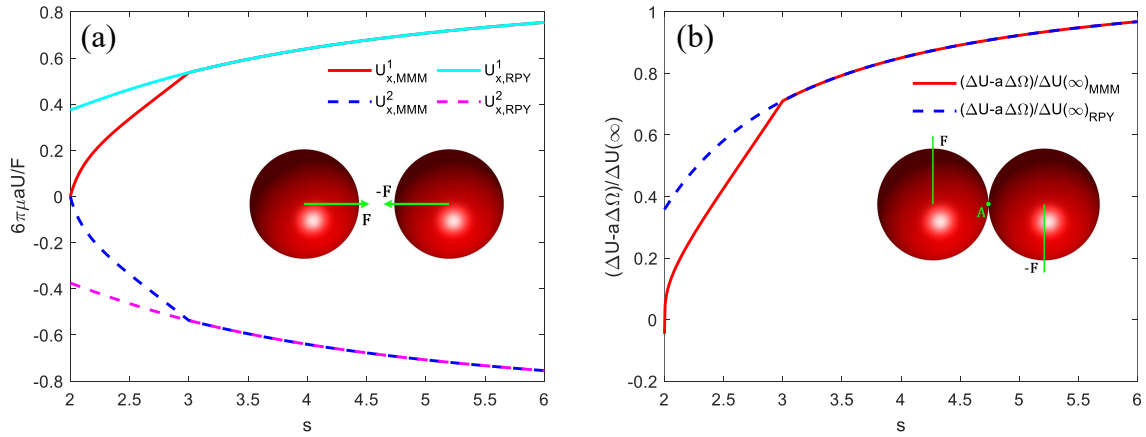


Figure 6. (a) The translational velocities of two equal spheres dragged by force \mathbf{F} and $-\mathbf{F}$ along the x -axis versus the reduced separation distance s . (b) The velocity difference of two equal spheres dragged by force \mathbf{F} and $-\mathbf{F}$ along the y -axis versus the reduced separation distance s . The results are obtained by the multipole moment method (MMM) and the Rotne-Prager-Yamakawa (RPY) tensor, respectively.

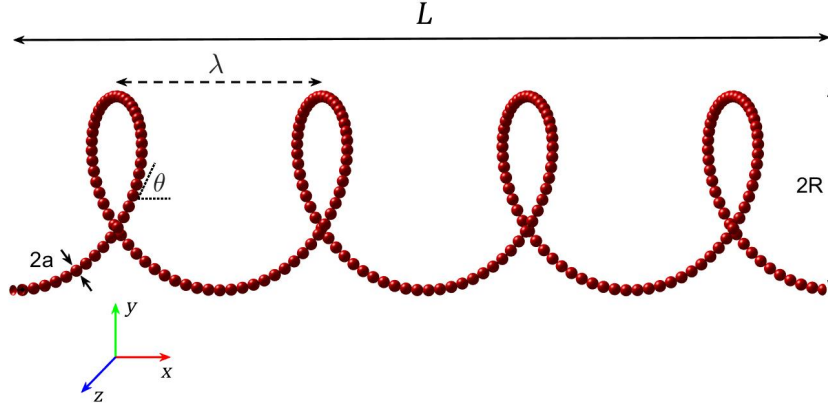


Figure 7. Schematic diagram of a helical flagellum model. The helical radius of the flagellum is R , helical pitch is λ , axial length is L , filament radius is a , contour length is $\Lambda = L/\cos\theta$, and the pitch angle is θ , where $\tan\theta = 2\pi R/\lambda$. The inset shows the direction of the coordinate system.

3. Propulsion of a Helical Rigid Flagellum

In order to assess the general accuracy and capabilities of the grand resistance matrix, the propulsion of a helical rigid flagellum is simulated and compared with Rodenborn's work[34]. A helical flagellum can be modeled as a rigid rotating helix with radius R , pitch λ , axial length L , pitch angle θ , filament radius a , contour length $\Lambda = L/\cos\theta$, and wave number $k = 2\pi/\lambda$, where $\tan\theta = 2\pi R/\lambda$. We consider a rigid bacterial flagellum as a string of spheres embedded in a viscous fluid and represent it as a helical sequence of N spheres, as shown in Figure 7. The centerline of the left-handed helical flagellum is given as follows:

$$\mathbf{r}(s) = (x, y, z) = [-x, \cos(kx - \omega t), \sin(kx - \omega t)]. \quad (12)$$

where $x = s \cos\theta$ and $s \in [0, \Lambda]$ and k is the helix wave number. The helical flagellum is divided into N equal discrete spheres with radius a , then, the translational velocity \mathbf{U} and rotational velocity $\mathbf{\Omega}$ related to the forces \mathbf{F} and \mathbf{T} exerted on the fluid are

$$\begin{pmatrix} \mathbf{F} \\ \mathbf{T} \end{pmatrix} = \mathcal{R} \begin{pmatrix} \mathbf{U} \\ \mathbf{\Omega} \end{pmatrix}. \quad (13)$$

Axial thrust F and torque T for a rotating, non-translating flagellum can be calculated from the above equation. The helical radius R is used as the unit of length; thrust and torque are made dimensionless by dividing by $\mu\Omega R^2$ and $\mu\Omega R^2$. Our results computed for the thrust F and torque T for a helical flagellum with radius $a = R/16$ are shown in Figure 8 as a function of the helical pitch λ ; the axial length is $L = 20R$. The total axial thrust $F = \sum_{i=1}^N |\mathbf{f}_i \cdot \mathbf{e}_x|$ and torque $T = \sum_{i=1}^N |[\mathbf{n}_i + (\mathbf{r}_i - \mathbf{r}_1) \times \mathbf{f}_i] \cdot \mathbf{e}_x|$, where \mathbf{f}_i and \mathbf{n}_i are the force and torque applied to the sphere i by the fluid, respectively.

The flagella are slender, and their filament radius a is much smaller than other geometric parameters. Resistive force theory[35, 36], slender body theory[36], regularized Stokeslet method[37, 38], boundary element method[39], and immersed boundary method[40] are often used for numerical simulations. Our results agree with Rodenborn's laboratory measurement and the numerical simulations conducted using the slender body theory and regularized Stokeslet method. The slender body theory and Regularized Stokeslet method, however, only couple force and translational velocity. For an elastic rod model or spheres immersed in viscous fluid, torque must be considered, and these two methods are unavailable.

We also constructed the grand resistance matrix by $\mathcal{R} = \mathcal{R}_{2B}^\infty + \mathcal{R}_{2B, \text{lub}}$, however, the result is far different from Rodenborn's result, which is almost an order of magnitude apart. This result examines that the term $(\mathcal{M}^\infty)^{-1}$ includes the far-field interactions between all spheres.

4. Summary and Conclusions

We have developed a new technique to construct the resistance and mobility matrix that takes account of both the near-field lubrication and far-field hydrodynamic interactions of a set of rigid spheres of arbitrary size immersed in a viscous fluid. The far-field mobility matrix \mathcal{M}^∞ only considers long-range hydrodynamic interactions, and the formulation is exactly the same as the Rotne-Prager-Yamakawa tensor. To include lubrication, we first invert \mathcal{M}^∞ to obtain a far-field approximation to the grand

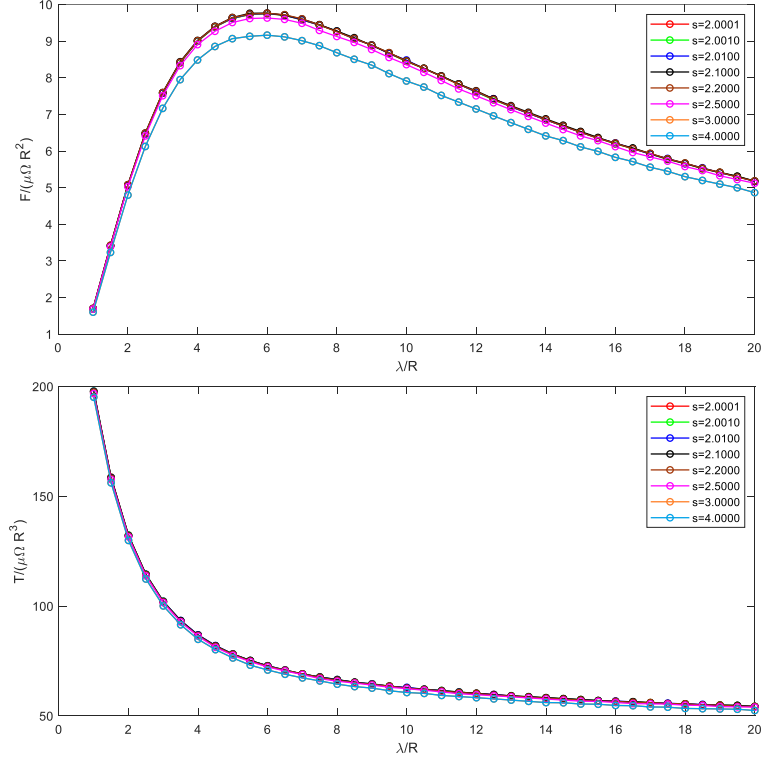


Figure 8. Dimensionless thrust and torque for the helical flagellum as a function of pitch λ (relative to the helix radius R) for helix length $L = 20R$ and filament radius $a = R/16$ for various values of s .

resistance matrix \mathcal{R} . This multi-sphere approximation to the grand resistance matrix still lacks lubrication, however. To include lubrication, we introduce it in a pairwise additive fashion $\mathcal{R}_{2B,lub}$ in the grand resistance matrix. However, the lubrication is only available for $\xi \leq \min\{\lambda, 1/\lambda\}$. Thus, our approach to the grand resistance matrix \mathcal{R} , which contains both near-field lubrication and far-field multi-sphere interactions, is $\mathcal{R} = (\mathcal{M}^\infty)^{-1} + \mathcal{R}_{2B,lub}$. Once the grand resistance matrix \mathcal{R} is obtained, the grand mobility matrix can be obtained by inverting it, $\mathcal{M} = (\mathcal{R})^{-1}$.

We consider a rotating, non-translating helical rigid flagellum, which is divided into a set of N identical, uniformly spaced spheres. Our calculations of axial thrust and torque for the flagellum with different pitches are presented in Figure 8. This procedure has given excellent results for different s compared to Rodenborn's work. To illustrate the effect of the inter-sphere separation distance, different s models are calculated. The grand resistance matrix constructed here captures both near- and far-field physics and has given excellent results for $2.0001 \leq s \leq 4.0000$ situations. This conclusion shows that the selection of s for a rigid filament model has little influence on the calculation results, which is crucial for our future work.

Our technique for constructing the grand resistance matrix has three main merits: it avoids overlap, satisfies the no-slip boundary condition, and includes all long-range terms. Our method can be easily extended to compute the grand resistance and mobility matrix for arbitrary-size spheres. While this method is accurate and efficient, it is still computationally intensive. The construction of a near-field lubrication resistance matrix requires $O(N^2)$ operations. The multi-sphere interactions obtained by inverting the mobility matrix in the grand resistance matrix require $O(N^3)$ operations and limit the size of systems that can be studied. This method does not consider the flow field around the sphere, and we will present a method in our next work to investigate the flow field around spheres.

Acknowledgments

We acknowledge computational support from Beijing Computational Science Research Center. This work was supported by the National Natural Science Foundation of China (NSFC) (Grant No. U2230402) and China Postdoctoral Science Foundation (Grant No. 2022M712927).

Appendix A. The scalar resistance and mobility functions

We follow the notation of Jeffrey and Onishi, define the variables $s = 2r/(a_\alpha + a_\beta)$, $\xi = s - 2$ and $\lambda = a_\beta/a_\alpha$ (the subscripts α , and β indicate the labels of the spheres), where r is the center-to-center distance of the inter-sphere and a_α is the radius of the sphere α . The scalar resistance functions for $\xi \leq \min\{\lambda, 1/\lambda\}$ are:

1. The scalar resistance functions X^a

$$\begin{aligned} X_{\alpha\alpha}^a &= g_1(\lambda)\xi^{-1} + g_2(\lambda)\ln(\xi^{-1}), \\ X_{\alpha\beta}^a &= -\frac{2}{1+\lambda} [g_1(\lambda)\xi^{-1} + g_2(\lambda)\ln(\xi^{-1})]. \end{aligned} \quad (14)$$

where

$$g_1(\lambda) = 2\lambda^2(1+\lambda)^{-3}, \quad g_2(\lambda) = \frac{1}{5}\lambda(1+7\lambda+\lambda^2)(1+\lambda)^{-3}. \quad (15)$$

2. The scalar resistance functions Y^a

$$\begin{aligned} Y_{\alpha\alpha}^a &= g_2(\lambda)\ln(\xi^{-1}), \\ Y_{\alpha\beta}^a &= -\frac{2}{1+\lambda} [g_2(\lambda)\ln(\xi^{-1})]. \end{aligned} \quad (16)$$

where

$$g_2(\lambda) = \frac{4}{15}\lambda(2+\lambda+2\lambda^2)(1+\lambda)^{-3}. \quad (17)$$

3. The scalar resistance functions Y^b

$$\begin{aligned} Y_{\alpha\alpha}^b &= g_2(\lambda)\ln(\xi^{-1}), \\ Y_{\alpha\beta}^b &= -\frac{4}{(1+\lambda)^2} [g_2(\lambda)\ln(\xi^{-1})]. \end{aligned} \quad (18)$$

where

$$g_2(\lambda) = -\frac{1}{5}\lambda(4+\lambda)(1+\lambda)^{-2}. \quad (19)$$

4. The scalar resistance functions X^c

$$\begin{aligned} X_{\alpha\alpha}^c &= 1, \\ X_{\alpha\beta}^c &= 0. \end{aligned} \quad (20)$$

5. The scalar resistance functions Y^c

$$\begin{aligned} Y_{\alpha\alpha}^c &= g_2(\lambda)\ln(\xi^{-1}), \\ Y_{\alpha\beta}^c &= g_4(\lambda)\ln(\xi^{-1}). \end{aligned} \quad (21)$$

where

$$g_2(\lambda) = \frac{2}{5}\lambda(1+\lambda)^{-1}, \quad g_4(\lambda) = \frac{4}{5}\lambda^2(1+\lambda)^{-4}. \quad (22)$$

The scalar mobility functions are:

$$\begin{aligned} x_{\alpha\alpha}^a &= 1, & x_{\alpha\beta}^a &= 3/2s^{-1} - (2+2\lambda^2)/(1+\lambda)^2s^{-3}, \\ y_{\alpha\alpha}^a &= 1, & y_{\alpha\beta}^a &= 3/4s^{-1} + (1+\lambda^2)/(1+\lambda)^2s^{-3}, \\ y_{\alpha\alpha}^b &= 0, & y_{\alpha\beta}^b &= -1/2s^{-2}, \\ x_{\alpha\alpha}^c &= 1, & x_{\alpha\beta}^c &= s^{-3}, \\ y_{\alpha\alpha}^c &= 1, & y_{\alpha\beta}^c &= -1/2s^{-3}. \end{aligned} \quad (23)$$

The sphere labels α and β can be interchanged.

References

- [1] John Happel and Howard Brenner. *Low Reynolds number hydrodynamics: with special applications to particulate media*, volume 1. Springer Science & Business Media, 2012.
- [2] Daisuke Takagi, Jérémie Palacci, Adam B Braunschweig, Michael J Shelley, and Jun Zhang. Hydrodynamic capture of microswimmers into sphere-bound orbits. *Soft Matter*, 10(11):1784–1789, 2014.
- [3] Sambeeta Das, Astha Garg, Andrew I Campbell, Jonathan Howse, Ayusman Sen, Darrell Velegol, Ramin Golestanian, and Stephen J Ebbens. Boundaries can steer active janus spheres. *Nature communications*, 6(1):8999, 2015.
- [4] Knut Drescher, Raymond E Goldstein, Nicolas Michel, Marco Polin, and Idan Tuval. Direct measurement of the flow field around swimming microorganisms. *Physical Review Letters*, 105(16):168101, 2010.
- [5] Roseanna N Zia, James W Swan, and Yu Su. Pair mobility functions for rigid spheres in concentrated colloidal dispersions: Force, torque, translation, and rotation. *The journal of chemical physics*, 143(22):224901, 2015.
- [6] Tzer Han Tan, Alexander Mietke, Junang Li, Yuchao Chen, Hugh Higinbotham, Peter J Foster, Shreyas Gokhale, Jörn Dunkel, and Nikta Fakhri. Odd dynamics of living chiral crystals. *Nature*, 607(7918):287–293, 2022.
- [7] Bokai Zhang, Premkumar Leishangthem, Yang Ding, and Xinliang Xu. An effective and efficient model of the near-field hydrodynamic interactions for active suspensions of bacteria. *Proceedings of the National Academy of Sciences*, 118(28):e2100145118, 2021.
- [8] Kiyoshi Kanazawa, Tomohiko G Sano, Andrea Cairoli, and Adrian Baule. Loopy lévy flights enhance tracer diffusion in active suspensions. *Nature*, 579(7799):364–367, 2020.
- [9] Jeremie Palacci, Stefano Sacanna, Asher Preska Steinberg, David J Pine, and Paul M Chaikin. Living crystals of light-activated colloidal surfers. *Science*, 339(6122):936–940, 2013.
- [10] Charles M Schroeder, Eric SG Shaqfeh, and Steven Chu. Effect of hydrodynamic interactions on dna dynamics in extensional flow: Simulation and single molecule experiment. *Macromolecules*, 37(24):9242–9256, 2004.
- [11] Davide Loi, Stefano Mossa, and Leticia F Cugliandolo. Non-conservative forces and effective temperatures in active polymers. *Soft Matter*, 7(21):10193–10209, 2011.
- [12] Rémi Dreyfus, Jean Baudry, Marcus L Roper, Marc Fermigier, Howard A Stone, and Jérôme Bibette. Microscopic artificial swimmers. *Nature*, 437(7060):862–865, 2005.
- [13] D. J. Jeffrey and Y. Onishi. Calculation of the resistance and mobility functions for two unequal rigid spheres in low-reynolds-number flow. *Journal of Fluid Mechanics*, 139:261–290, 1984.
- [14] D. J. Jeffrey. The calculation of the low reynolds number resistance functions for two unequal spheres. *Physics of Fluids A: Fluid Dynamics*, 4(1):16–29, 1992.
- [15] D. J. Jeffrey, J. F. Morris, and J. F. Brady. The pressure moments for two rigid spheres in low-reynolds-number flow. *Physics of Fluids A: Fluid Dynamics*, 5(10):2317–2325, 1993.
- [16] Jens Rotne and Stephen Prager. Variational treatment of hydrodynamic interaction in polymers. *The Journal of Chemical Physics*, 50(11):4831–4837, 1969.
- [17] Hiromi Yamakawa. Transport properties of polymer chains in dilute solution: hydrodynamic interaction. *The Journal of Chemical Physics*, 53(1):436–443, 1970.
- [18] Richard M Jendrejack, David C Schwartz, Michael D Graham, and Juan J de Pablo. Effect of confinement on dna dynamics in microfluidic devices. *The Journal of chemical physics*, 119(2):1165–1173, 2003.
- [19] Richard M Jendrejack, David C Schwartz, Juan J De Pablo, and Michael D Graham. Shear-induced migration in flowing polymer solutions: Simulation of long-chain dna in microchannels. *The Journal of chemical physics*, 120(5):2513–2529, 2004.
- [20] Tadashi Ando and Jeffrey Skolnick. On the importance of hydrodynamic interactions in lipid membrane formation. *Biophysical journal*, 104(1):96–105, 2013.
- [21] Eligiusz Wajnryb, Krzysztof A Mizerski, Pawel J Zuk, and Piotr Szymczak. Generalization of the rotne–prager–yamakawa mobility and shear disturbance tensors. *Journal of Fluid Mechanics*, 731, 2013.
- [22] Krzysztof A Mizerski, Eligiusz Wajnryb, Pawel J Zuk, and Piotr Szymczak. The rotne-prager-yamakawa approximation for periodic systems in a shear flow. *The Journal of chemical physics*, 140(18):184103, 2014.

- [23] Louis Durlafsky, John F Brady, and Georges Bossis. Dynamic simulation of hydrodynamically interacting particles. *Journal of fluid mechanics*, 180:21–49, 1987.
- [24] John F Brady and Georges Bossis. Stokesian dynamics. *Annual review of fluid mechanics*, 20:111–157, 1988.
- [25] Louis J Durlafsky and John F Brady. Dynamic simulation of bounded suspensions of hydrodynamically interacting particles. *Journal of Fluid Mechanics*, 200:39–67, 1989.
- [26] Andreas Zöttl and Julia M Yeomans. Enhanced bacterial swimming speeds in macromolecular polymer solutions. *Nature Physics*, 15(6):554–558, 2019.
- [27] Aitor Martín-Gómez, Thomas Eisenstecken, Gerhard Gompper, and Roland G Winkler. Active brownian filaments with hydrodynamic interactions: conformations and dynamics. *Soft Matter*, 15(19):3957–3969, 2019.
- [28] Eric Lauga, Michael P Brenner, and Howard A Stone. Microfluidics: the no-slip boundary condition. *arXiv preprint cond-mat/0501557*, 2005.
- [29] Rémi Dreyfus, Jean Baudry, Marcus L Roper, Marc Fermigier, Howard A Stone, and Jérôme Bibette. Microscopic artificial swimmers. *Nature*, 437(7060):862–865, 2005.
- [30] Bradley J Nelson, Ioannis K Kaliakatsos, and Jake J Abbott. Microrobots for minimally invasive medicine. *Annual review of biomedical engineering*, 12:55–85, 2010.
- [31] Sangtae Kim and Seppo J Karrila. *Microhydrodynamics: principles and selected applications*. Courier Corporation, 2005.
- [32] Eric Lauga and Thomas R Powers. The hydrodynamics of swimming microorganisms. *Reports on progress in physics*, 72(9):096601, 2009.
- [33] Tamar Schlick and Wilma K Olson. Trefoil knotting revealed by molecular dynamics simulations of supercoiled dna. *Science*, 257(5073):1110–1115, 1992.
- [34] Bruce Rodenborn, Chih-Hung Chen, Harry L. Swinney, Bin Liu, and H. P. Zhang. Propulsion of microorganisms by a helical flagellum. *Proceedings of the National Academy of Sciences*, 110(5):E338–E347, 2013.
- [35] James Gray and GJ Hancock. The propulsion of sea-urchin spermatozoa. *Journal of Experimental Biology*, 32(4):802–814, 1955.
- [36] James Lighthill. Flagellar hydrodynamics. *SIAM review*, 18(2):161–230, 1976.
- [37] Ricardo Cortez. The method of regularized stokeslets. *SIAM Journal on Scientific Computing*, 23(4):1204–1225, 2001.
- [38] Ricardo Cortez, Lisa Fauci, and Alexei Medovikov. The method of regularized stokeslets in three dimensions: analysis, validation, and application to helical swimming. *Physics of Fluids*, 17(3):031504, 2005.
- [39] DJ Smith, EA Gaffney, JR Blake, and JC Kirkman-Brown. Human sperm accumulation near surfaces: a simulation study. *Journal of Fluid Mechanics*, 621:289–320, 2009.
- [40] Sookkyung Lim, Anca Ferent, X Sheldon Wang, and Charles S Peskin. Dynamics of a closed rod with twist and bend in fluid. *SIAM Journal on Scientific Computing*, 31(1):273–302, 2008.